RESEARCH

Space/ground-borne techniques and petrographic microscopic dissection for geologic mapping in Gabal Ras Abda area, Northeastern Desert, Egypt

Mahmoud M. Salem[1], Mohamed A. Yehia[2], Ali A. Omran[1], Hassan I. El Sundoly[1], Mohammed A. Soliman[1] and Karim Abdelmalik[2*]

Abstract

Background Gabal Ras Abda area as a part of the Red Sea Mountain range, is characterized by inaccessible and rugged terrains. The exposed rock units are hardly followed in the field because of the rigid topography. Thus, the present work proposes and develops an integrated approach to map the exposed rock units and extract the geologic structures using satellite imagery data followed by both field and petrographic verification, saving time, efforts and cost.

Results To achieve the target, both the measured spectral signature curves with Landsat-8 and Sentinel-2A data were used to develop and create the most enhanced Band Ratios and Principal Components for lithological discrimination and mapping which were (((Band7 + Band 4)/(Band 7), (Band 2)/(Band 2 + Band 5) and (Band 5) in RGB) and ((Band 9 + Band 11 + Band 12)/(Band 1), (Band 4 − Band 2) and (Band 11/Band 6) + (Band 6) in RGB)) with Principal Component Bands ((PC1, PC2 and PC3 in RGB) and (PC3, PC2 and PC1 in RGB)), respectively. Also, georeferenced Google Earth Pro, panchromatic band of Landsat-8 and ALOS PALSAR Digital Elevation Model images were used to extract the structural lineaments. Geologic, petrographic and field structural studies were emphasized the remote sensing results, indicating that the main rock types cropped out in Ras Abda area from the oldest to the youngest are older granitoids (quartz-diorites, tonalites and granodiorites), Dokhan volcanics (andesites, rhyodacites, rhyolites and their related tuffs), younger gabbros, younger granites (monzogranites, syenogranites and alkali-feldspar granites), post-granite dykes and offshoots (acidic, microgranitic and basic types) and Phanerozoic sedimentary rocks. Also, the study emphasized that the E-W trend is the main structural trend controlling the investigated area followed by WNW-ESE and NE-SW directions.

Conclusions The results of remote sensing achieved compliance with the geologic, petrographic and structural investigation through distinctly differentiating the different rocks and extracting the lineaments, indicating the accuracy of the remote sensing results and emphasizing their importance and effective role in producing a precise and highly accurate geologic map.

Keywords Band ratio, Principal component analysis, Lineament extraction, Geologic mapping, Ras Abda
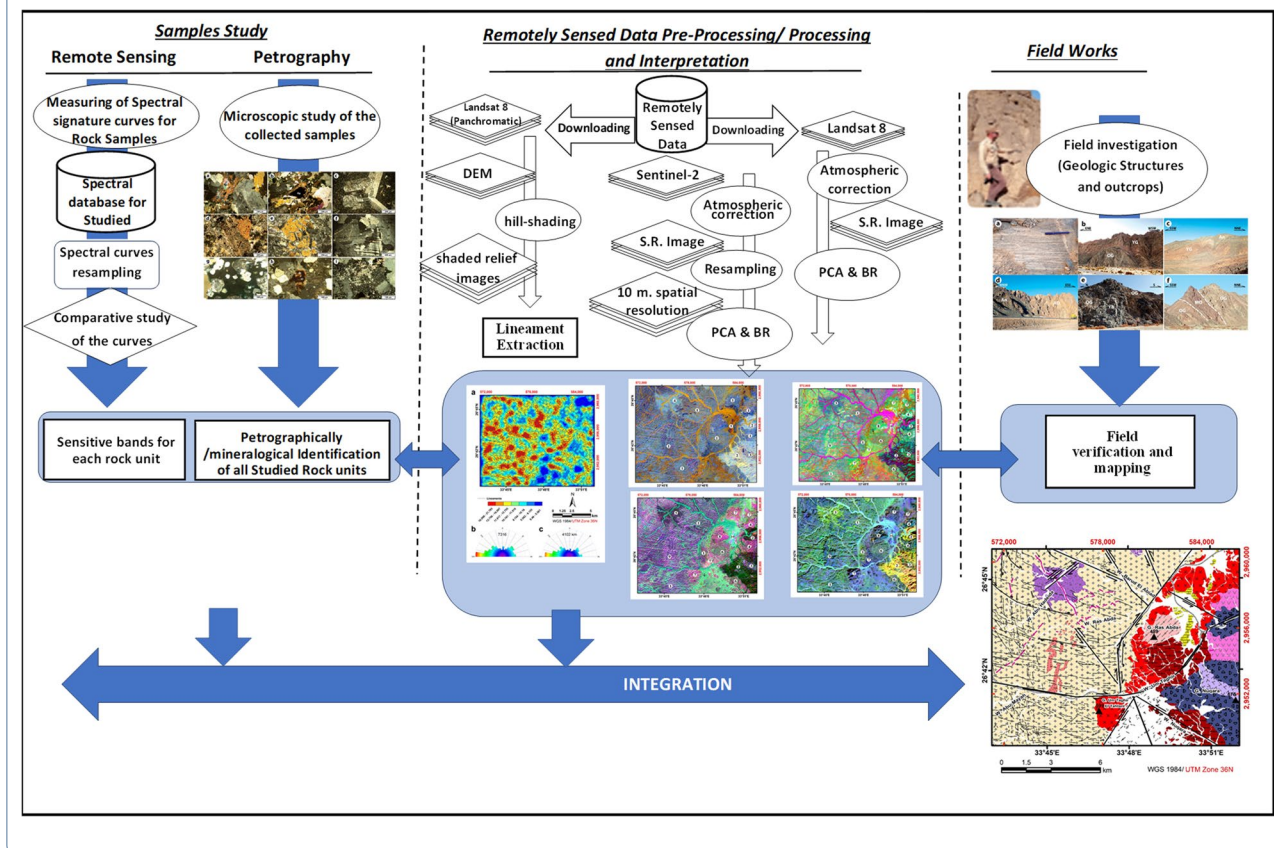
*Correspondence:
Karim Abdelmalik
Karim.abdelmalik@sci.asu.edu.eg
Full list of author information is available at the end of the article

Salem *et al. Beni-Suef Univ J Basic Appl Sci*   (2024) 13:44

Page 2 of 22

Graphical abstract

1 Background

The Arabian-Nubian Shield (ANS) is related to the northern segment of the Pan-African orogenic belt of East Africa [32], considering to be one of the best preserved and most widely exposures of Neoproterozoic juvenile continental crust on Earth [13, 24]. It is composed of island arc volcanosedimentary sequences and I-type magmatic rocks (plutonic and volcanic) that were derived from oceanic island arc volcanism and cratonized during the continental collision between the East and West Gondwana that closed the Mozambique Ocean and induced the East African Orogeny (EAO) around 750–630 Ma [4, 35]. After cratonization, the shield is injected by the eruption of K-rich volcanic rocks and emplacement of granitoid intrusions [18]. Then, these rocks are exposed on the both flanks of the Red Sea in the western Arabia and northeastern Africa after uplift and erosion during Oligocene and younger times [27, 35].

The investigated area constitutes a part of the northwestern ANS. It is composed of older granitoids, younger gabbros and younger granites which dissected by acidic, granitic and basic dykes of different attitudes [31]. Awad et al. [5] classified the investigated granites into tonalites, granodiorites, monzogranites and alkali-feldspar granites. El-Mansi et al. [17] reported that the present Dokhan volcanics are related to fissure-type eruption and are classified as intermediate (basaltic andesites and andesites) and acidic volcanics (rhyolites and rhyodacites).

The study area is located at the extreme southern part of the northeastern desert (NED) of Egypt with a part at the central eastern desert (CED), nearby the Red Sea coast at about 10 km west Safaga City. It is bounded by latitudes 26° 39′ 30″–26° 46′ 00″ N and longitudes 33° 43′ 00″–33° 52′ 00″ E, covering an area of about 180 km^2 (Fig. 1a). It can be easily accessible from Safaga City on the Red Sea coast through Qena-Safaga asphaltic road, which passes through the southern part of the study area. It is dissected by several complex wadis with their tributaries—most of them are structurally controlled—e.g., Wadi (W.) Um Taghir striking E to NE, W. Abu Mayah (ENE to NE), W. Nuqara (SE), W. Ras Abda (ENE to E), W. Abu Hadeida (NE) and W. Barud El Abiad (E to ESE), while the highest peaks are represented by Gabal (G.) Nuqara (814 m above sea level), G. Um Taghir El Tahtani
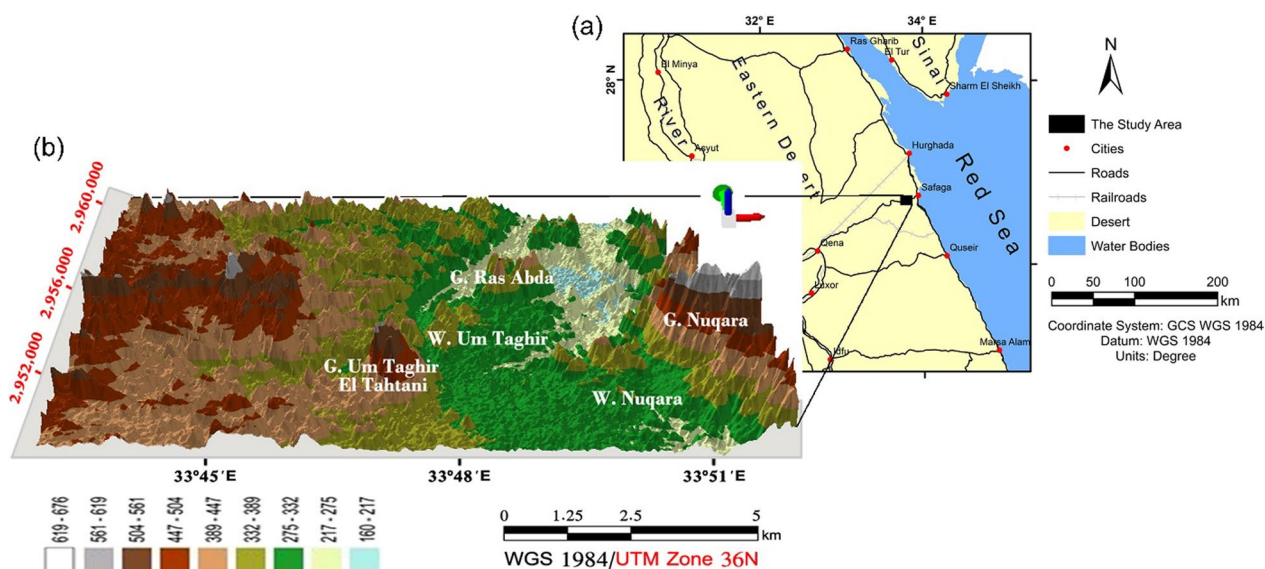
Salem *et al. Beni-Suef Univ J Basic Appl Sci* (2024) 13:44

Page 3 of 22

Fig. 1 **a** Location map of G. Ras Abda area, northeastern desert, Egypt. **b** 3D topographic model showing the main wadis and mountains in the study area

(599 m) and G. Ras Abda (459 m), occupying the eastern and southern parts (Fig. 1b).

Qena-Safaga road (W. Um Taghir) is considered the Egypt's largest fault shear zone separating two tectono-stratigraphic domains: NED and CED [15]. The NED—northern and central parts of the study area—is dominated by extensional structures with E-W and NE-SW main tectonic trends which were controlled by the evolution and retreat of the Cadomian Arc, while the CED—southern parts—is modified by transpressional and extensional structures with NW–SE and WNW-ESE main tectonic trends which kinematically akin to the Najd Orogeny [25]. This is the main reason for selecting this area as a point of research.

Undoubtedly, the remotely sensed data application has brought new opportunities for the lithological identification and lineament extraction, particularly in inaccessible and rugged terrains, as in the case with the study area. In this respect, many studies used satellite imagery data for lithological discrimination and mineral exploration (e.g., [1, 7, 21, 33]) and for lineament extraction and structural analysis (e.g., [11, 14, 30]) to create an accurate geologic map. The present paper is addressed to differentiate the exposed rock types in Ras Abda area using the remote sensing technique via integration between the rocks' spectral signature curves and remotely sensed data of Landsat-8 and Sentinel-2A. It is also concerned with the structural lineament extraction to elucidate the main trend controlling the study area. Obtained rock types and structural lineaments are geologically and petrographically verified on the field and under the polarizing

microscope, respectively, in order to produce a precise geologic map of the study area.

2 Methods

2.1 Satellite imagery data

2.1.1 Landsat data

Landsat-8 OLI/TIRS C1 Level 1TP (Path 174/Row 42) is the data used, obtained from the home site of Earth Explorer (https://earthexplorer.usgs.gov/), and acquired on December 14, 2020, at the day time according to the date of field trip (from 9 to 16 December 2020), with cloud cover equals about zero. Landsat-8 launched on February 11, 2013, carrying two sensors; the Operational Land Imager (OLI) and the Thermal Infrared Sensor (TIRS) to offer regular visible, infrared and thermal images of high quality, where the OLI measures in the Visible/Near Infrared (VNIR) and Short-Wave Infrared (SWIR) portions of the spectrum for nine spectral bands, and the TIRS measures land surface temperature in two thermal bands (Table 1).

2.1.2 Sentinel data

Sentinel Level 2A S2MSI2A is the data used, obtained from the home page of ESA Hub (https://scihub.copernicus.eu/dhus/), and acquired on December 11, 2020, with cloud coverage assessment is about 0.1%. Sentinel-2 based on a constellation of two identical satellites in the same orbit: Sentinel-2A and Sentinel-2B. Each satellite carries an innovative wide swath high-resolution Multispectral Imager (MSI) which measures in the Visible/Near Infrared (VNIR) and Short-Wave Infrared (SWIR)

Salem *et al. Beni-Suef Univ J Basic Appl Sci* (2024) 13:44

Page 4 of 22

Table 1 Spectral characteristics and spatial resolutions of Sentinel-2 bands and Landsat-8

Sentinel-2				Landsat-8			
Band #	Wavelength Window (nm)	Resolution (m)	Band Name	Band #	Wavelength Window (nm)	Resolution (m)	Band Name
B1	433.9–453.9	60	Coastal Aerosol	B1	430–450	30	Coastal Aerosol
B2	464.1–529.1	10	Blue	B2	450–510	30	Blue
B3	542.5–577.5	10	Green	B3	530–590	30	Green
B4	649.5–679.5	10	Red	B4	640–670	30	Red
B5	696.4–711.4	20	Vegetation Red Edge				
B6	732.7–747.7	20	Vegetation Red Edge				
B7	772.5–792.5	20	Vegetation Red Edge				
B8	777.6–892.6	10	NIR				
B9	854.8–874.8	20	Narrow NIR	B5	850–880	30	NIR
B10	935–955	60	Water Vapor				
B11	1358.5–1388.5	60	SWIR–Cirrus	B9	1360–1380	30	Cirrus
B12	1568.7–1658.7	20	SWIR	B6	1570–1650	30	SWIR 1
B13	2112.4–2292.4	20	SWIR	B7	2110–2290	30	SWIR 2
				B8	500–680	15	Panchromatic
				B10	10,600–11,190	100	TIRS 1
				B11	11,500–12,510	100	TIRS 2

regions of the spectrum with thirteen spectral bands for providing a systematic optical imagery at high spatial resolution over land, vegetation and coastal areas. Sentinel-2 is the most advanced satellite with data freely available for long-range and high-frequency remote sensing applications, so it is one of the used materials in the current study (Table 1). The Landsat-8 and Sentinel-2A data geometrically corrected and georeferenced to Universal Traverse Mercator (UTM) Zone 36N map projection (units: meters) and to World Geodetic System 1984 (WGS84) datum and ellipsoid.

2.1.3 Laboratory spectral measurements

Understanding the interaction behavior between the Electromagnetic Radiation (EMR) and the targets considered as a major key factor in the processing and/or interpretation. Therefore, spectral signature is used as an effective method where it plots all the variations of reflected or emitted EMR of a material with respect to wavelengths (i.e., reflectance/emittance as a function of wavelength). Many authors used the relation between measured spectral signature curves with the remotely sensed imagery to discriminate and map the different rock types (e.g., [2, 3, 20, 21]).

Spectral signature of ten suitable samples, representative of all the exposed rock types in the study area, was measured by an ASD TerraSpec Halo Mineral Identifier with the wavelength range of 0.35 μm to 2.5 μm. Averages of the spectral reflectance data are subjected to resampling algorithm to match wavelengths of Landsat-8 and

Sentinel-2A bands. Then from the matched values, curves of the reflectance are plotted and carefully examined to detect the most sensitive bands, which are defined as a peak between two adjacent troughs or a trough between two adjacent peaks. Using sensitive bands, the optimal and appropriate band ratios and band math are generated and developed to accurately discriminate the studied rock types.

2.2 Image pre-processing and processing
2.2.1 Atmospheric correction
Ideally, satellite imagery that is recorded by a remote sensing system considers the result of the reflectance of visible and infrared electromagnetic waves from the Earth's surface. These reflected signals comprise the actual reflectance from the surface and atmospheric noise resulted from effect of the atmosphere as well as errors which may be introduced by the sensor system itself. So that it is necessary to exclude these errors from data before image processing by executing some pre-processing corrections in order to get an accurate result.

Herein, the Fast Line-of-sight Atmospheric Analysis of Spectral Hypercubes (FLAASH) algorithm is applied to retrieve Landsat-8 image data from radiance to reflectance. This process is mainly based on some parameters, e.g., acquisition time, sun elevation, ground elevation, gains, offsets, solar irradiance, atmospheric model and aerosol model to determine Top-Of-Atmosphere reflectance (TOA), then calculate the Surface Reflectance (SR). ENVI 5.3 software package is used for pre-processing

Salem *et al. Beni-Suef Univ J Basic Appl Sci*   (2024) 13:44

Page 5 of 22

and processing of the data, and ArcMap 10.2 software is used for the final editing.

Although band rationing does not need the SR values, the authors executed the atmospheric correction for two reasons:

1. To correlate the actual measured reflectance of represented rock samples with the SR values in the corrected images.
2. For further research which will include some methods need to use the SR values—such as target detection—and integrate the results with subsurface geophysical data in order to develop a three-dimensional map of the investigated targets.

2.2.2 Pixel resampling
Sentinel-2A is pre-corrected atmospherically, but it includes thirteen spectral bands with different spatial resolution ranging from 60 to 10 m, so all bands with resolution of 20 and 60 m are spatially resampled to the smallest pixel-meter size (e.g., band 2 of 10 m) using ESA SNAP 8.0 software to preserve the spectral characteristics of the resampled bands.

2.2.3 Band ratios (BR)
BRs are approaches of image processing that are done by combining the pixels of two or more raster layers in mathematical combinations to enhance the spectral differences between bands and reduce the topographic illumination effects. Vincent [36] stated that band ratios are used to improve compositional information and exclude the other types such as terrain slope and grain size differences. This process is widely applied in geologic and mineral mapping (e.g., [10, 12, 16, 19, 23, 26]).

2.2.4 Principal component analysis (PCA)
Principal component transform is a multivariate linear statistical procedure for removing redundant spectral information from multiband datasets in order to simplify these datasets from multidimensional to lower dimensions of uncorrelated linear combinations (eigenvector loadings) [22, 29]. PCA colored images show the maximum variance from several spectral bands with just compressed three primary display colors [36].

An eigenvector matrix displays the statistical correlation between the PCs and the input bands indicating the proportion that each input band contributes to each PC in what is known as weighting or factor loading. Eigenvalues indicate the proportion of original information that each PC retains. From eigenvalues, the percentage of the total variance for each PC can be calculated by computing the ratio of each eigenvalue to the sum of all of them.

2.2.5 Structural lineament extraction
Linear features may represent man-made/artificial features such as roads, railroads, tracks, aqueducts, or natural morphologic ones such as shear zones, faults, joints, dykes, veins, fold axial traces, ridgelines, truncation of outcrops, rift valleys and surface depressions in addition to topographic, vegetation and soil tonal changes alignment. Natural geologic linear features are often related to structural discontinuities of rocks and tectonic activity named structural lineaments. Digital Elevation Models (DEMs) and satellite images are extensively used for structural lineament extraction (e.g., [6, 34]), where they are considered to be better tools to discriminate the lineaments and produce better information than conventional methods; furthermore, they make lineaments extraction easier, time saver and cheaper than them. In the current study, two methods of extracting lineaments are used:

2.2.5.1 Manual lineament extraction This method involves manual digitizing of visually identified lineaments depending on human experience and ability, so it is easy to distinguish the kind of lineaments (natural or artificial). Georeferenced google earth image of maximum resolution and ArcMap 10.2 software are used to extract lineaments manually.

2.2.5.2 Automated lineament extraction Conversely, this technique is automated lineament extraction using the mathematical function and specified algorithms of software cannot recognize the kind of lineaments. Panchromatic band of landsat-8 (15 m) and ALOS PALSAR DEM (12.5 m) is used.

2.3 Field and microscopic data
Field studies were carried out in G. Ras Abda area to check the occurrence and spatial distribution of the different rock types and the contacts between them, and to measure the different structural elements (faults, joints, dykes and veins). The collected samples for spectral signature were used again to petrographically study the rocks under the polarizing microscope in the NMA laboratories.

2.3.1 Fault data
The considerable area is highly dissected by numerous faults of different types, attitudes and extensions depending on the causative stress tensors and strength properties of the rock material. A number of 2122 field faults (fault plane with slicklines) of different conjugate systems

Salem *et al. Beni-Suef Univ J Basic Appl Sci*   (2024) 13:44

Page 6 of 22

were measured and statistically analyzed using Win-Tensor 2013 software [8].

2.3.2 Joint data

A number of 787 joints measured in all rock types are also statistically treated and plotted on a composite rose diagram in order to determine the main joint trends based on the frequency of their distribution in number proportions (*N*%).

2.3.3 Dyke and vein data

The attitudes of 224 dykes and veins were measured in the field and traced on the satellite image. They are statistically treated and graphically represented to illustrate their main trends.

3 Results

3.1 Satellite imagery interpretation

3.1.1 Band ratios (BR)

Image processing is a method to perform some operations on a digital image in order to enhance the appearance of the imagery to assist in visual interpretation, analysis and extraction of some useful information from it. This image enhancement involves many techniques

determined mainly based on the target of the study, the type of image format, the initial condition of the image and the composition of the image scene. In the present study, band ratio and principal component analysis are applied.

Both measured and resampled spectral signature curves are thoroughly studied to determine their reflectance behavior as well as the sensitive bands in order to create the optimum band ratios and combinations to enhance satellite images and accurately distinguish between the different rock types in the investigated area. Regarding to measured spectral signature curves of the represented samples (Fig. 2) and resampled Landsat-8 curves (Fig. 3), five bands (b4, b5, b6, b7 and b8) are selected as the most sensitive ones for the studied rock types. Two band ratios (Eqs. 1 and 2) were developed and created using the selected sensitive bands; the band ratio images show the best differentiation of the rock units in the study area. The band ratio images resulted by applying Eqs. 1 and 2 were stacked with b5 and displayed in RGB, respectively. The resulted image represented different wavelengths (2 and 4 of visible red and blue, 5 of NIR and 7 of SWIR); thus, it gave the highest variance discriminating among all the present rock types (Fig. 4).
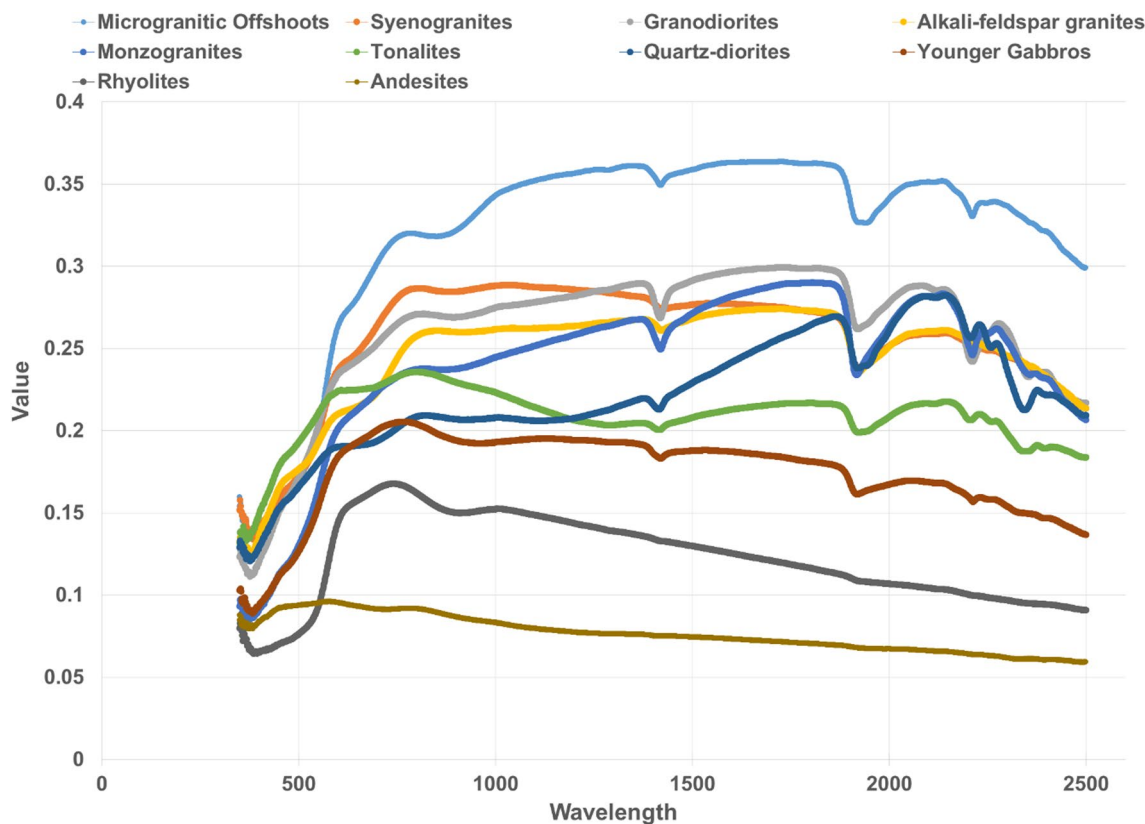

Fig. 2 ASD TerraSpec Laboratory measured spectral curves of the studied rock samples
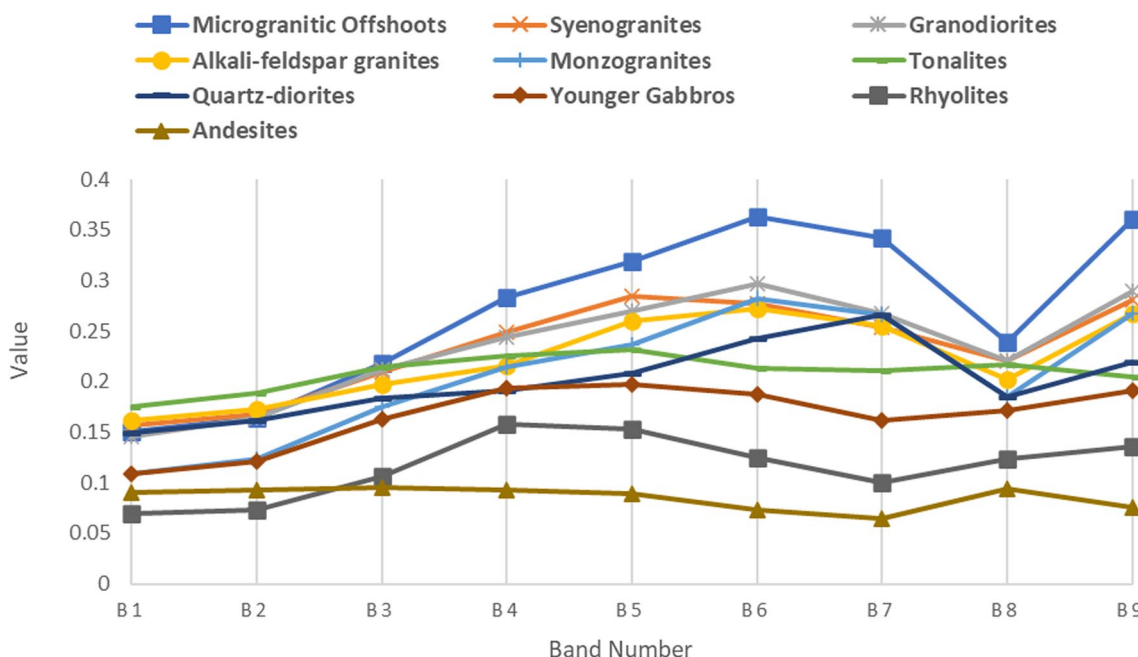
Salem *et al. Beni-Suef Univ J Basic Appl Sci*   (2024) 13:44

Page 7 of 22

Fig. 3 Resampled Landsat-8 spectral curves of the studied rock samples

$$\frac{\text{Band 7} + \text{Band 4}}{\text{Band 7}} \qquad (1)$$

$$\frac{\text{Band 2}}{\text{Band 2} + \text{Band 5}} \qquad (2)$$

On the other hand, the measured spectral signature curves of the represented samples (Fig. 2) and resampled Sentinel-2A curves (Fig. 5) indicated four bands (b2, b4, b9 and b11) as the most sensitive ones. Accordingly, three band ratios are developed (Eqs. 3, 4 and 5) and then stacked in false color composite image to clearly distinguish between all the investigated rock types (Fig. 6).

$$\frac{\text{Band 9} + \text{Band 11} + \text{Band 12}}{\text{Band 1}} \qquad (3)$$

$$(\text{Band 4}) - (\text{Band 2}) \qquad (4)$$

$$\left(\frac{\text{Band 11}}{\text{Band 6}}\right) + \text{Band 6} \qquad (5)$$

3.1.2 Principal component analysis (PCA)

Landsat-8 bands are subjected to PCA (eigenmatrix shown in Table 2), and the eigenvectors show that the highest variant and the lowest redundant pixel values are between PC1, PC2 and PC3 (Table 3). So that the three PCs are combined in RGB image to characterize all the exposed rock types in the considerable area (Fig. 7). Likewise, Sentinel-2A is subjected to PCA (eigenmatrix shown in Table 4), displaying PC1, PC2 and PC3 are the highest variant PCs (Table 5), so the colored image of PC3 in red, PC2 in green and PC1 in blue is the most appropriate image to discriminate between the examined rock types (Fig. 8).

3.1.3 Structural lineament extraction

3.1.3.1 Manual lineament extraction   A structural lineament density map which displays the distribution and concentration of the lineaments over the study area in order to highlight areas with the prevalence of structures was produced (Fig. 9a). Afterward, the extracted lineaments are subjected to geometric calculation to obtain polyline angles which are integrated in RockWorks 2016 to create rose diagrams based on both their number and cumulative length proportions showing the main trends of lineaments (Fig. 9b, c). The resulted rose diagrams revealed that the most common lineament trends are E–W, WNW–ESE and NE–SW in descending manner followed by NW–SE and ENE–WSW trends, while NNE–SSW, N–S and NNW–SSE represent the least common trends.

3.1.3.2 Automated lineament extraction   To make edge enhancement, panchromatic band of landsat-8 (15 m) is
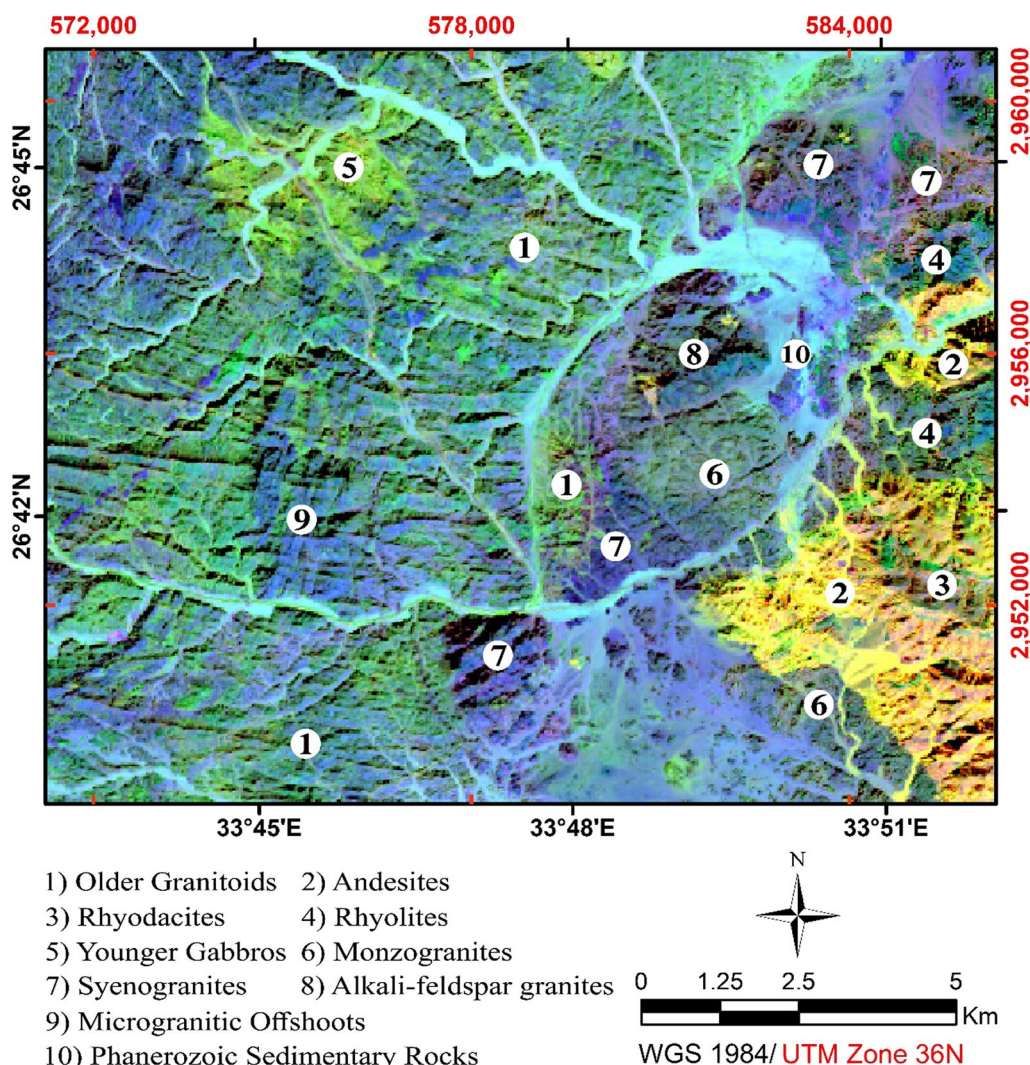
Fig. 4 False color Landsat-8 band ratios composite ((b7 + b4)/(b7), (b2)/(b2 + b5) and (b5) in RGB) of the studied rock types

subjected to directional filtering process by using ENVI 5.3 at eight directional filter angles (0°/360°, 45°, 90°, 135°, 180°, 225°, 270° and 315°) producing eight enhanced edge gray-scale images. Lineaments are automatically extracted from each image by using the Lineament Extraction (LINE) algorithm of PCI Geomatica 2013 software. Then, the extracted lines are merged and splitized to produce lineament density map (Fig. 10a), and rose diagrams are built based on their frequency and length proportions (Fig. 10b, c) indicating that E-W is the abundant trend followed by WNW–ESE, ENE–WSW, NE–SW and NNE–SSW trending. This is besides NW–SE, N–S and NNW–SSE as minor trends.

Also, ALOS PALSAR DEM (12.5 m) is subjected to hill-shading procedure by using ArcMap 10.2 at eight solar angles (0°/360°, 45°, 90°, 135°, 180°, 225°, 270° and 315°) and sun height equals 45. Eight separated shaded

relief images are resulted. Each image is submitted to LINE algorithm and the extracted lines from eight images are merged and splitized to make lineament density map (Fig. 11a) and plotted in rose diagrams (Fig. 11b, c). E−W direction represents the predominant lineament trend followed by WNW–ESE, NE–SW, NW–SE and ENE–WSW directions, while NNW–SSE, NNE–SSW and N–S represent the least abundant trends.

3.2 Field and microscopic verification
3.2.1 Rock-type discrimination
Ras Abda area is generally covered by the Neoproterozoic crystalline basement rocks, belonging to late- to post-orogenic magmatism (Continental crust terrain) which is dated to the Late Cryogenian-Ediacaran periods (650–542 Ma) [28]. The studied rocks are connected to igneous rocks of intrusive and extrusive types (older granitoids,
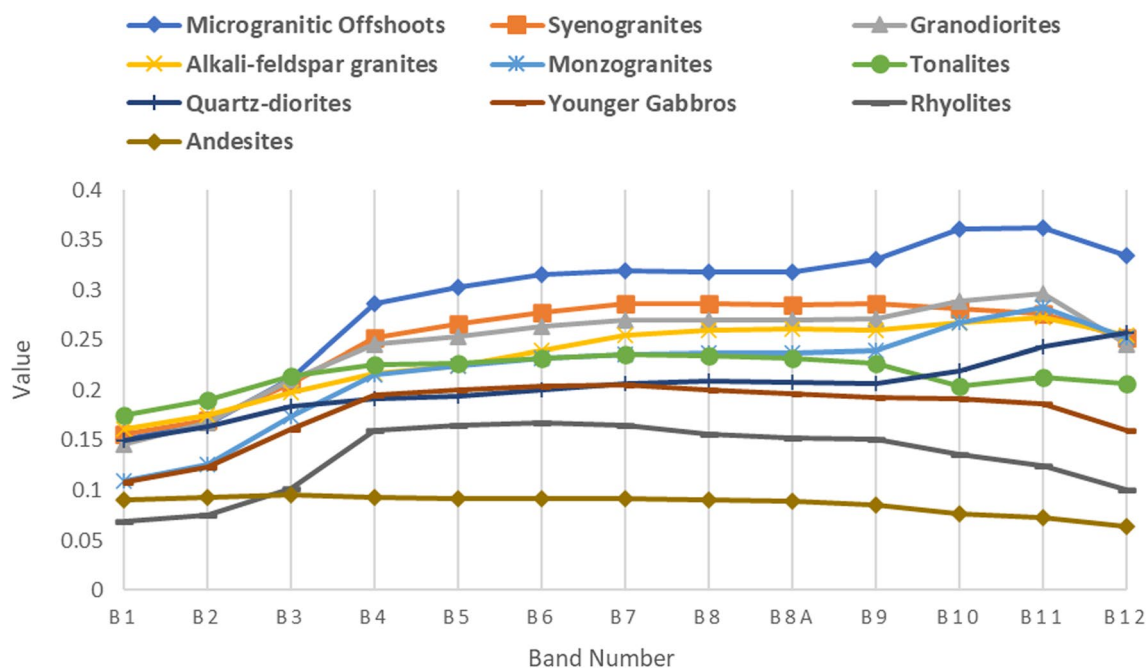
Salem *et al. Beni-Suef Univ J Basic Appl Sci*   (2024) 13:44

Page 9 of 22

Fig. 5 Resampled Sentinel-2A spectral curves of the studied rock samples

Dokhan volcanics, younger gabbros, younger granites and post-granite dykes and offshoots) in addition to few occurrences of Phanerozoic sedimentary sequences.

The older granitoids represent the oldest and most predominant rock type, covering about 92 km^2 (51.1%) of the total area. They are commonly medium- to coarse-grained, light gray in color and exhibit cavernous weathering, bouldery appearance and well-developed exfoliation. Gneissic and migmatitic structures are presented, especially along the peripheries (Fig. 12a). They are intruded by the younger gabbros and younger granites with sharp intrusive contacts (Fig. 12b), receiving many offshoots from them.

The Dokhan volcanics are well-exposed along the eastern parts of the study area as a part of G. Nuqara, showing moderate to high rugged topography with sharp pointed peaks and steep slopes. They are intruded by the younger granites with sharp intrusive contact, receiving several offshoots and apophyses from them and are carrying by them as roof-pendants (Fig. 12c). The present volcanics display two members of volcanic flow sheets and minor pyroclastics; lower intermediate (andesites) and upper acidic (rhyodacites and rhyolites) and their related tuffs (Fig. 12d). Andesites are intercalated with acidic volcanics in the form of three elongated parallel belts trending NW–SE. Andesites are very fine- to fine-grained, light gray to dark gray in color and include vesicles and amygdules filled with calcite, chlorite and quartz. Rhyodacites and rhyolites are very fine- to fine-grained,

faint to reddish pink in color and overlain by andesites enclosing xenoliths from them.

The younger gabbros are situated along the northern peripheries of W. Abu Hadeida with limited distribution. They are hard and compact rocks, fine- to medium-grained and dark gray in color, displaying cavernous weathering and bouldery appearance as well as spheroidal- and onion-shaped blocks. They intrude the surrounding older granitoids with sharp intrusive contact sending several offshoots into them (Fig. 12e) and carrying them as roof-pendants.

The younger granites are represented by an elongated curved belt extends NNE to NE from G. Um Taghir El Tahtani at the southern parts through G. Ras Abda in the middle to the northeastern limit of the study area. They are medium- to coarse-grained, varying in color from grayish pink, pink to reddish pink and sometimes display blocky appearance, spheroidal exfoliation and tuffoni weathering. They are classified into monzogranites, syenogranites and alkali-feldspar granites. Monzogranites are intruded by syenogranites which are intruded by alkali-feldspar granites with gradational contacts. Xenoliths of pre-existing rocks are recorded.

Post-granite dykes and offshoots involve acidic, microgranitic and basic types. The microgranites are cropped out along the two banks of W. Ras Abda at its middle part extending southward to W. Um Taghir as separated offshoots and elongated elliptical-shaped bodies with vertical walls, heterogeneous geometries and variable
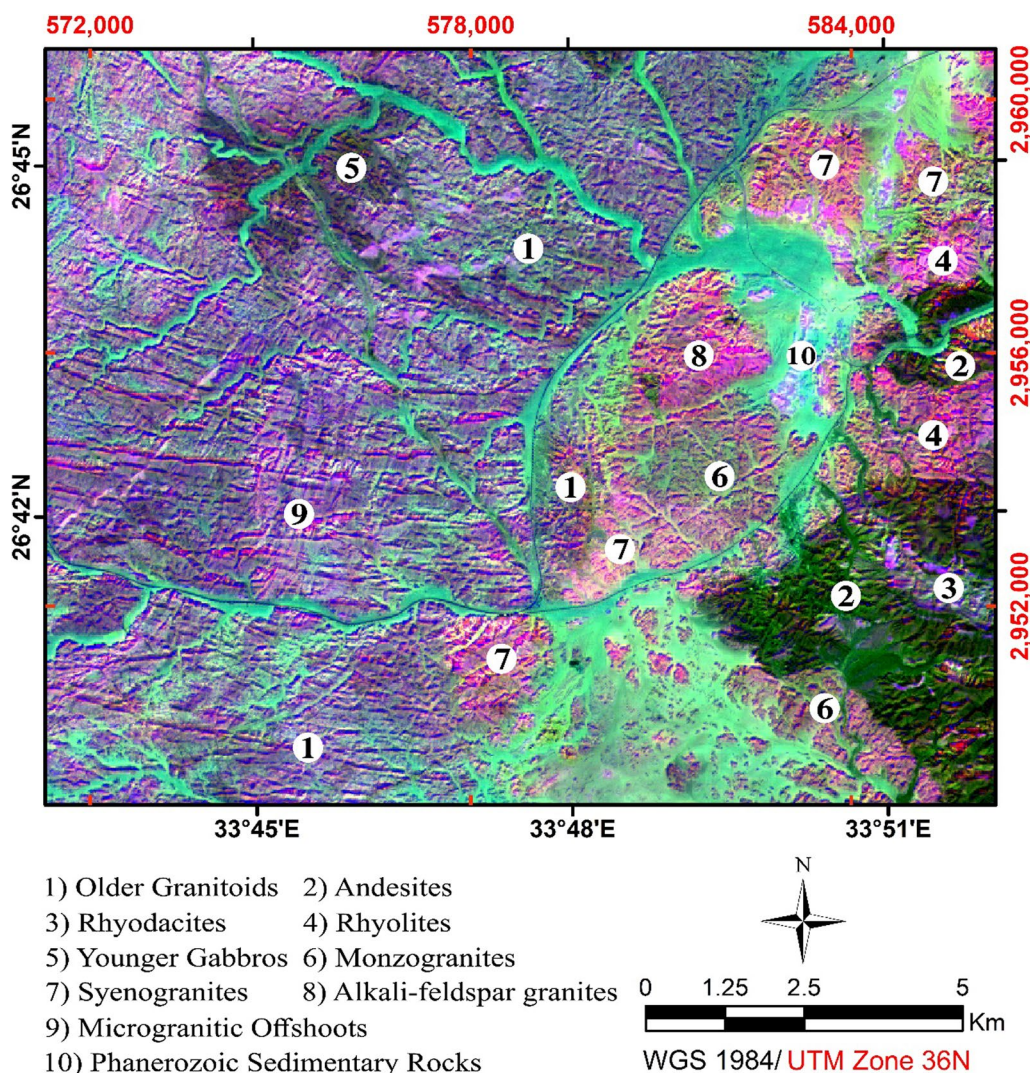
Fig. 6 False color Sentinel-2A band ratios composite ((b9 + b11 + b12)/(b1), (b4-b2) and (b11/b6) + (b6) in RGB) of the studied rock types

Table 2 PCA eigenmatrix for LandSat-8 data

	PC1	PC2	PC3	PC4	PC5	PC6	PC7
b1	0.154408	0.173696	0.278695	0.374747	0.436052	0.549684	0.485374
b2	−0.392277	−0.376402	−0.393474	−0.346596	−0.203305	0.419300	0.460808
b3	0.642997	0.363372	0.011869	−0.371679	−0.496597	0.161894	0.208353
b4	0.104894	0.020017	−0.180136	−0.218909	0.228023	0.625784	−0.681635
b5	−0.407744	0.058596	0.609909	0.146304	−0.561271	0.295905	−0.185291
b6	−0.323854	0.378597	0.347597	−0.681153	0.376111	−0.125833	0.098471
b7	−0.355940	0.740907	−0.492041	0.260758	−0.115921	0.028741	0.000881

magnitude from few to hundred meters in length and from less than a meter up to tens of meters in width trending NNE to NE. Dessouky et al. [9] reported that these dykes show significant complex morphological

feature as the first phenomenon to be recorded of this kind in the Egyptian Eastern Desert. They are fine- to medium-grained and show color varying from pink, dark red, reddish brown to brownish black according to their

Salem *et al. Beni-Suef Univ J Basic Appl Sci*   (2024) 13:44

Page 11 of 22

Table 3 PCA eigenvalues and total variance for Landsat-8 data

PC Bands	Eigenvalues	Total variance %
PC1	0.121034	98.772
PC2	0.001048	0.855
PC3	0.000248	0.202
PC4	0.000129	0.105
PC5	0.000063	0.051
PC6	0.000013	0.011
PC7	0.000004	0.003

alteration degrees. They are invaded the older granitoids (Fig. 12f), and in turn they are traversed by basic dykes with no evidence of their intruding by acidic ones, so that they are dated as post-acidic dykes and pre-basic dykes in age. The basic dykes as well as aplites, pegmatites and quartz veins cut all the earlier mentioned rock types.

Phanerozoic sedimentary rocks are unconformably capped all the studied basement rocks, particularly the Dokhan volcanics and younger granites at the northeastern parts, with very limited extension as mappable and unmappable low-lying hills and small sporadic masses of clastic, phosphate and carbonate rocks.

Petrographically, the older granitoids range in composition from quartz-diorites to granodiorites passing through tonalites. They are composed of various ratios of plagioclase (An_{18}–An_{42}) (Fig. 13a), quartz, hornblende and biotite with minor alkali-feldspar (microcline). Tonalites differ from quartz-diorites in being lighter in color, richer in quartz content and contain less hornblende and more alkali-feldspar and biotite. On the other hand, granodiorites only differ from tonalites in their
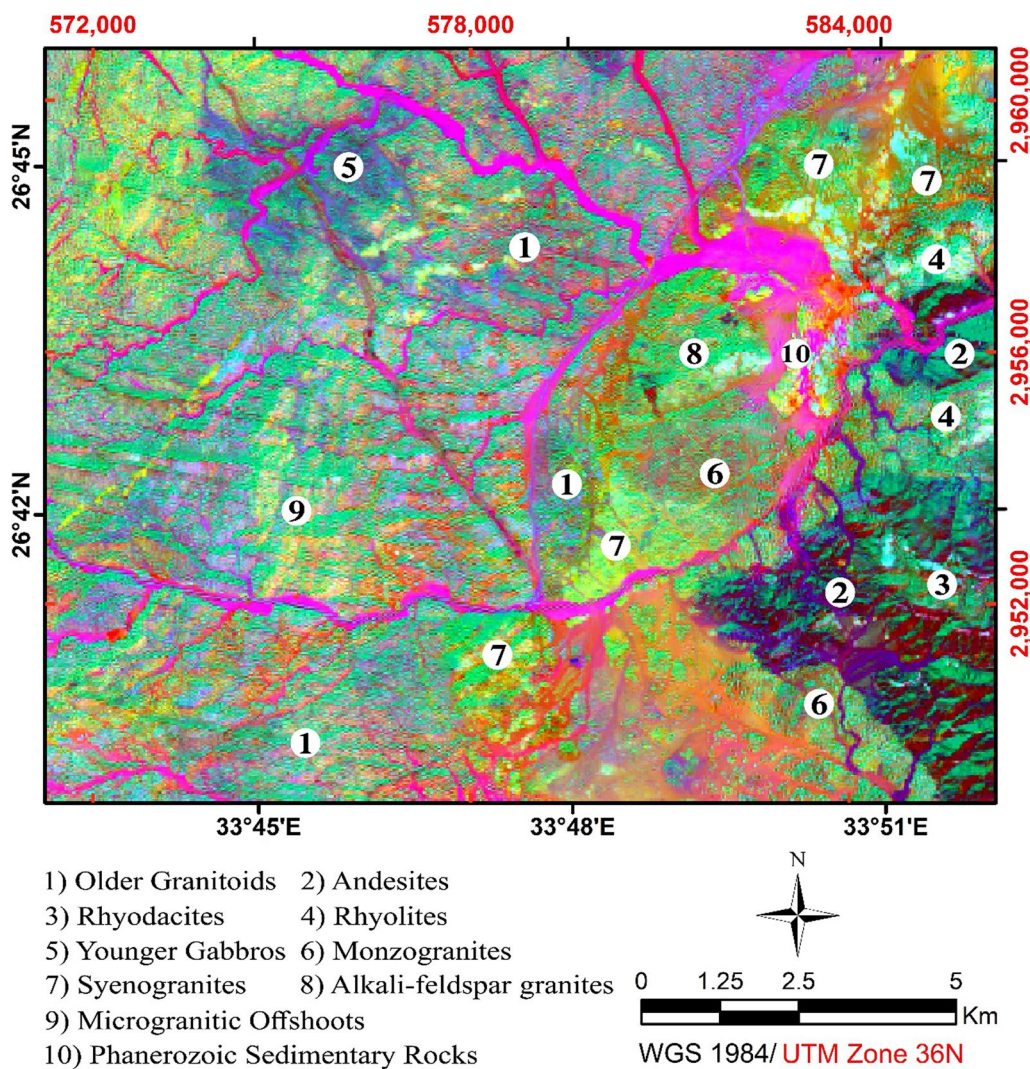

1) Older Granitoids   2) Andesites
3) Rhyodacites   4) Rhyolites
5) Younger Gabbros   6) Monzogranites
7) Syenogranites   8) Alkali-feldspar granites
9) Microgranitic Offshoots
10) Phanerozoic Sedimentary Rocks

WGS 1984/ UTM Zone 36N

Fig. 7 PCA color Landsat-8 bands composite (PC1, PC2 and PC3 in RGB) of the studied rock types

Table 4 PCA eigenmatrix for Sentinel-2A data

	PC1	PC2	PC3	PC4	PC5	PC6	PC7	PC8	PC9	PC10	PC11	PC12
b1	−0.088579	−0.161984	−0.224844	−0.299966	−0.317944	−0.319890	−0.322014	−0.337293	−0.320992	−0.246990	−0.358348	−0.334740
b2	−0.078430	0.320769	0.387564	0.394942	0.025927	0.004484	−0.019250	0.355298	−0.060102	−0.459543	−0.379231	−0.314425
b3	0.371732	0.109355	0.111172	0.084497	−0.021828	−0.032080	−0.042064	0.036391	−0.065709	0.750872	−0.323821	−0.390859
b4	−0.016828	0.095792	0.154132	0.213974	−0.421530	−0.395014	−0.380385	0.315089	−0.321320	0.163639	0.334629	0.318277
b5	−0.497459	−0.428708	−0.348863	0.122397	−0.128989	−0.003373	0.065840	0.516816	0.195339	0.180149	−0.044546	−0.267168
b6	0.116228	0.113243	0.059316	−0.090403	−0.086548	0.044154	−0.050475	−0.026514	0.088147	−0.116675	0.692835	−0.669240
b7	0.132774	0.053273	0.004266	−0.076971	−0.518570	0.584578	−0.419607	0.031380	0.394854	−0.046889	−0.129154	0.105359
b8	−0.546230	0.005366	0.174690	0.208314	0.171386	0.455522	−0.255936	−0.323082	−0.401372	0.217971	0.091714	−0.062540
b9	−0.499813	0.342625	0.378049	−0.408063	−0.069275	−0.297172	0.025084	−0.094634	0.422426	0.196603	−0.058556	0.011755
b10	−0.070779	−0.045742	0.039431	0.492084	−0.531551	−0.077324	0.495690	−0.448347	0.114721	0.020527	0.013969	−0.013000
b11	−0.030806	0.095806	0.117019	−0.459742	−0.332072	0.307500	0.504007	0.275950	−0.478639	0.014910	−0.014332	0.017144
b12	0.121621	−0.722211	0.670220	−0.092838	0.006380	−0.023373	−0.025634	−0.010161	0.046386	−0.046432	0.002959	−0.011904

Salem *et al. Beni-Suef Univ J Basic Appl Sci*   (2024) 13:44

Page 13 of 22

Table 5 PCA eigenvalues and total variance for Sentinel-2A data

PC bands	Eigenvalues	Total variance %
PC1	0.075821	94.392
PC2	0.002095	2.608
PC3	0.001200	1.494
PC4	0.000635	0.791
PC5	0.000266	0.331
PC6	0.000103	0.128
PC7	0.000059	0.073
PC8	0.000044	0.055
PC9	0.000039	0.049
PC10	0.000023	0.029
PC11	0.000022	0.027
PC12	0.000019	0.024

high content of alkali-feldspar and somewhat high content of quartz. Accessory minerals are represented by sphene, zircon, apatite and opaques (Fig. 13b). Epidote, chlorite, sericite, kaolinite and titanite represent the secondary minerals.

Andesites consist of plagioclase (An_{24}–An_{44}) and hornblende with subordinate amount of biotite and quartz as essential minerals. They usually exhibit porphyritic texture and sometimes glomeroporphyritic (Fig. 13c) and amygdaloidal ones. Rhyodacites and rhyolites comprise phenocrysts of alkali-feldspar (sanidine and orthoclase) and quartz with little amount of plagioclase, biotite and opaques set in a microcrystalline groundmass that mainly composed of the same minerals and mostly corroded them. Spherulitic and porphyritic textures are prevalent in these volcanic rocks (Fig. 13d).
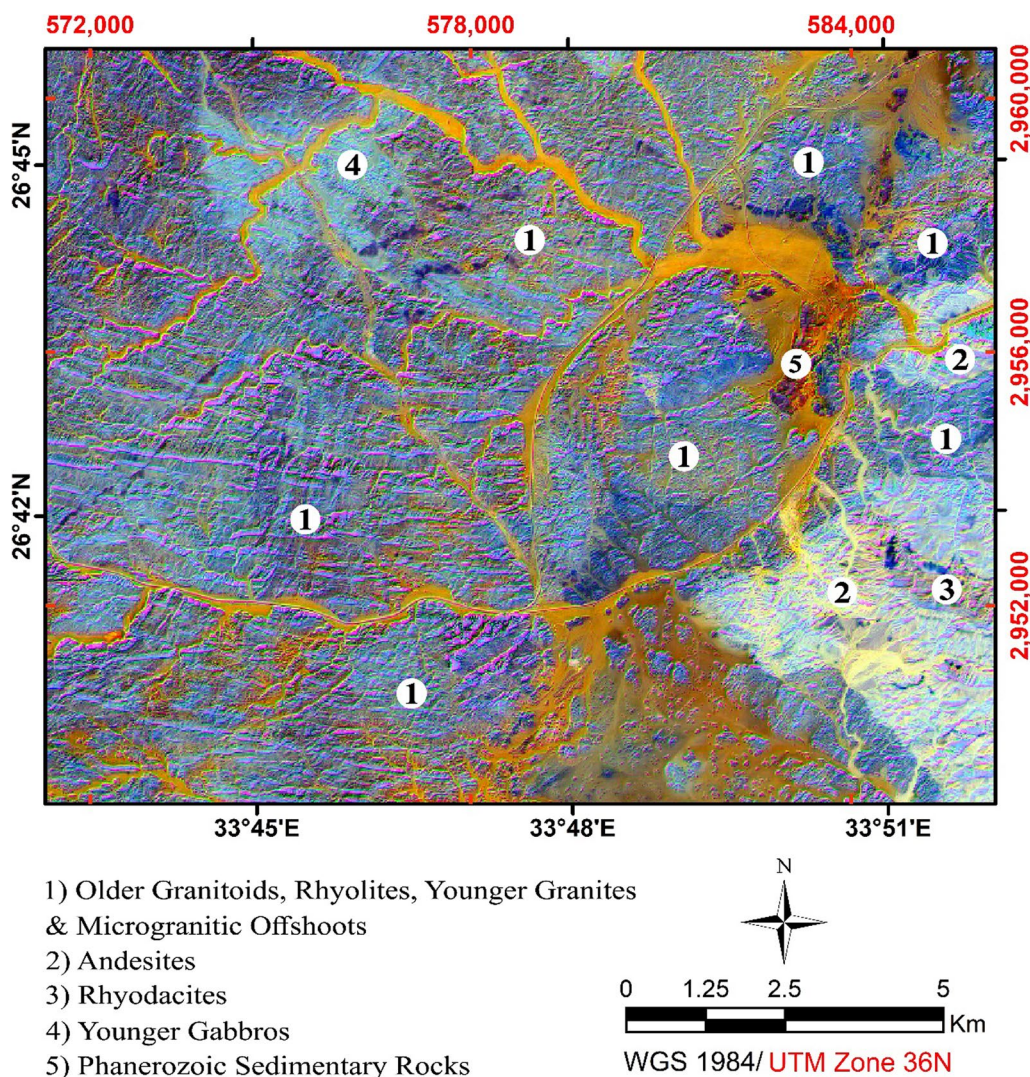

1) Older Granitoids, Rhyolites, Younger Granites & Microgranitic Offshoots
2) Andesites
3) Rhyodacites
4) Younger Gabbros
5) Phanerozoic Sedimentary Rocks

Fig. 8 PCA color Sentinel-2A bands composite (PC3, PC2 and PC1 in RGB) of the studied rock types

Salem *et al. Beni-Suef Univ J Basic Appl Sci*　　(2024) 13:44
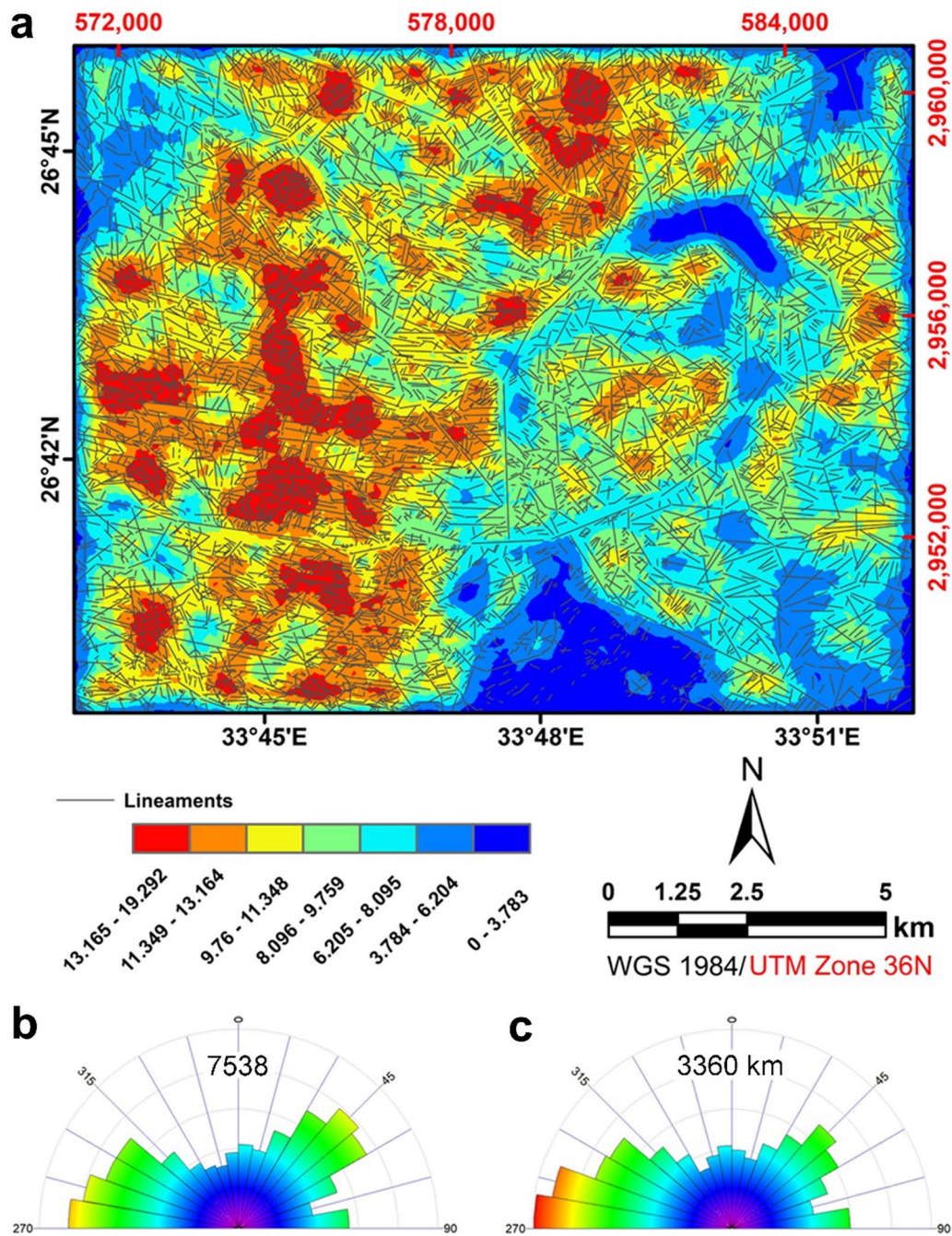
Page 14 of 22

Fig. 9 Manual lineament extraction, **a** lineament density map. **b** Rose diagram of lineament frequencies (*N%*). **c** Rose diagram of lineament lengths (*L%*)

The younger gabbros are predominantly composed of plagioclase (An_{55}-An_{70}), olivine, pyroxene (augite) and hornblende (Fig. 13e). Apatite and opaques represent the accessory minerals.

Monzogranites are mainly composed of orthoclase perthite, quartz, plagioclase (An_{14}–An_{35}), hornblende and appreciable amount of biotite, while syenogranites consist of perthite (orthoclase and microcline), quartz, plagioclase (An_{12}–An_{27}) with little amount of biotite (Fig. 13f), whereas alkali-feldspar granites are chiefly represented by orthoclase perthite, quartz, riebeckite (Fig. 13g), arfvedsonite and biotite with very little amount of albite and aegirine augite. Zircon, sphene, apatite, allanite and opaques are the accessories (Fig. 13h), while
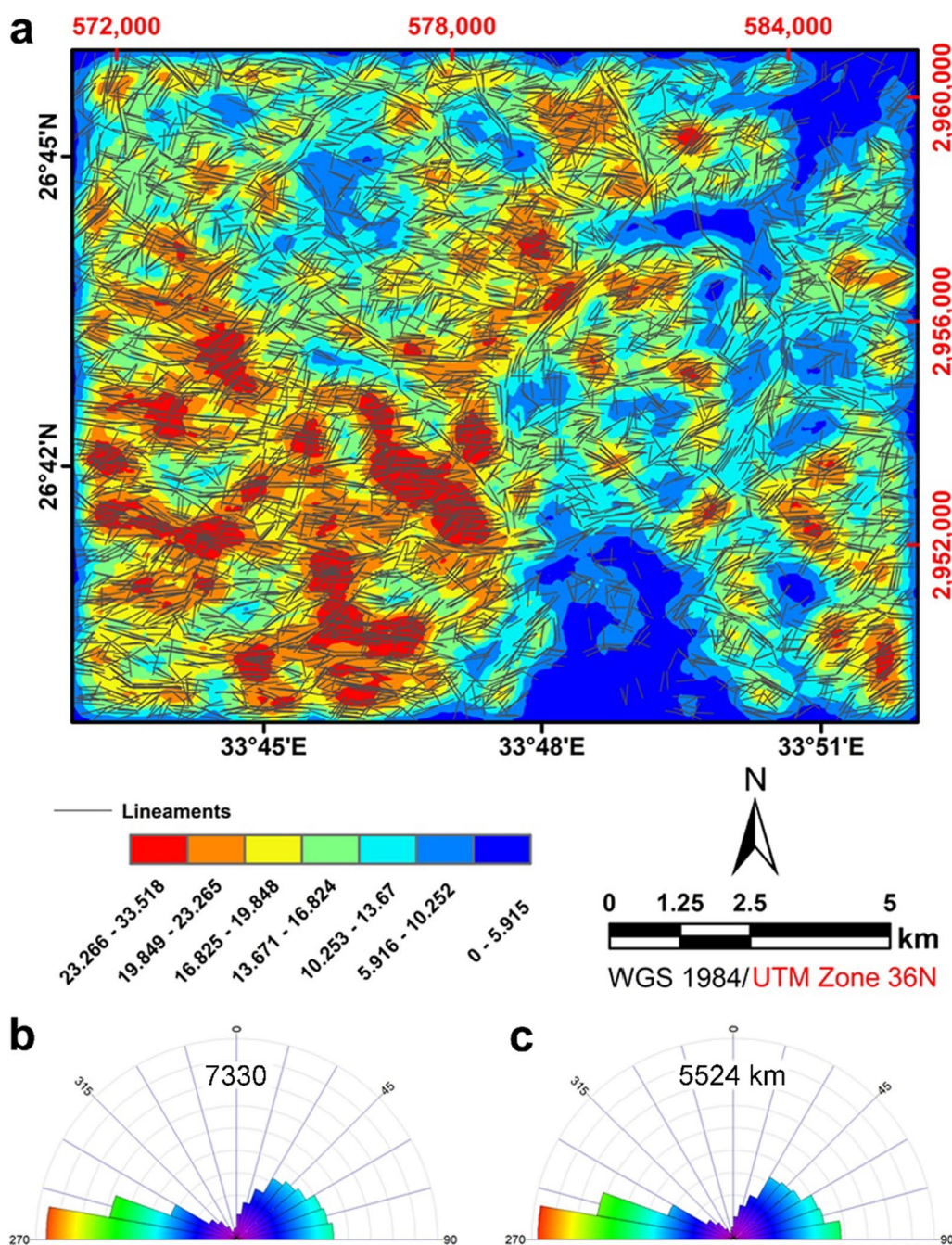
Fig. 10 Automated lineament extraction on panchromatic band of landsat-8 image, **a** lineament density map. **b** Rose diagram of lineament frequencies (*N*%). **c** Rose diagram of lineament lengths (*L*%)

titanite, epidote, chlorite, sericite and kaolinite represent the secondary minerals in the younger granites.

The microgranites are of syenogranitic composition and sometimes show alkali-feldspar granite varieties, consisting of alkali-feldspar (microcline, microcline perthite and orthoclase perthite), quartz, plagioclase (An_{13}–An_{28}) with little amount of biotite. They are highly charged with zircon, allanite, fluorite, sphene and iron oxides. Frequently, the microgranitic rock is highly hematitized and silicified (Fig. 13i).

3.2.2 Surface structural analysis
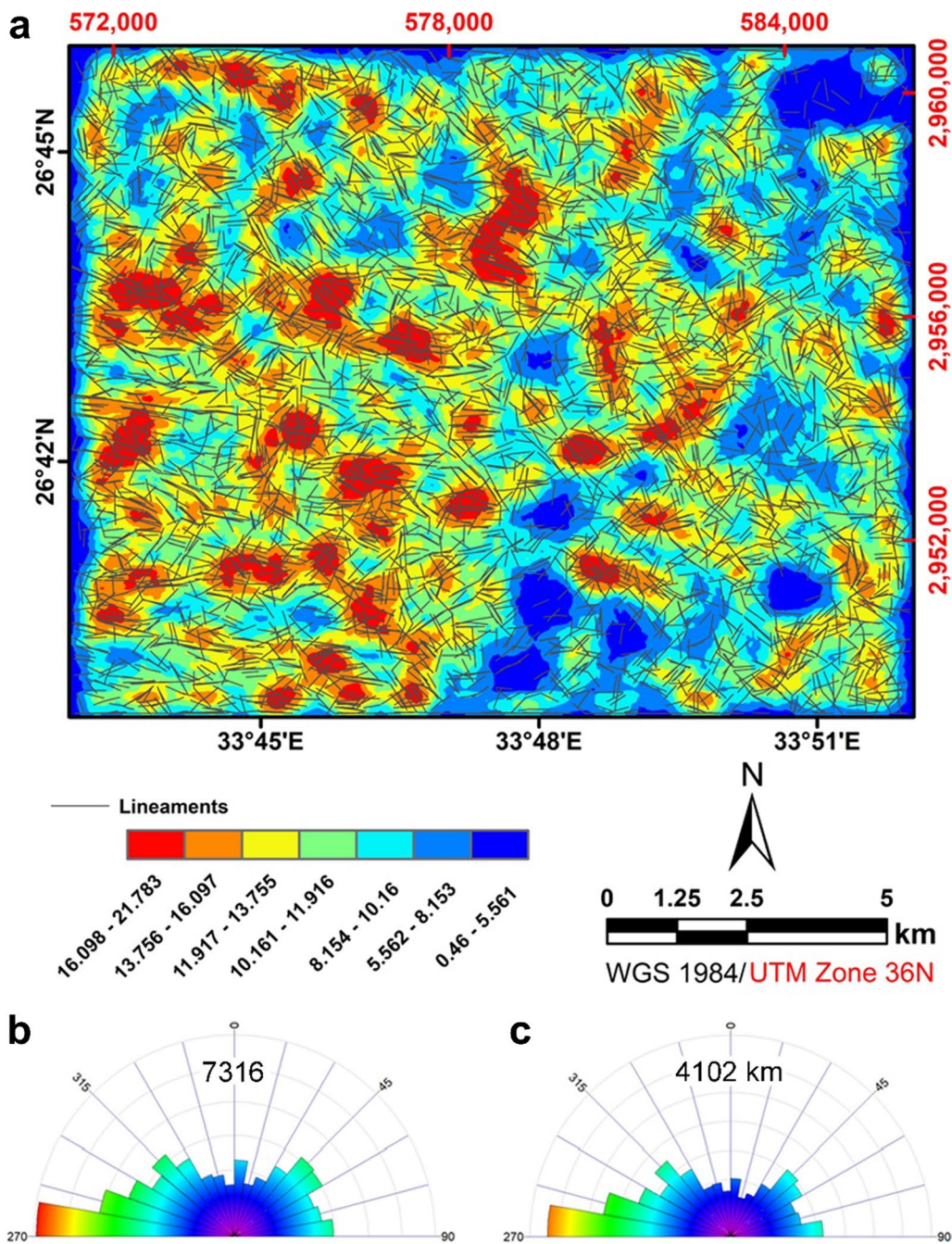*3.2.2.1 Fault analysis* The statistical analyses of the measured faults (Fig. 14) revealed that the main fault

Fig. 11 Automated lineament extraction on ALOS PALSAR DEM, **a** lineament density map. **b** Rose diagram of lineament frequencies (*N*%). **c** Rose diagram of lineament lengths (*L*%)

trends in the study area are WNW–ESE, ENE–WSW and NE–SW followed by E–W, NNE–SSW, NW–SE, N–S and NNW–SSE trends. The dip direction diagram indicated that ENE, ESE and NE are the abundant directions followed by E, N, SE, SSE, SSW, NNE and WSW directions. SW, S, WNW, NW, W and NNW represent the minor trends. Their dip angles are mostly very steep to nearly vertical angles followed by vertical ones, while steep to very steep angles are the least frequent. The slickenline rake angles showed that the horizontal and horizontal to nearly horizontal angles are the most common, while the gentle to moderate and moderate to steep angles are the least common.
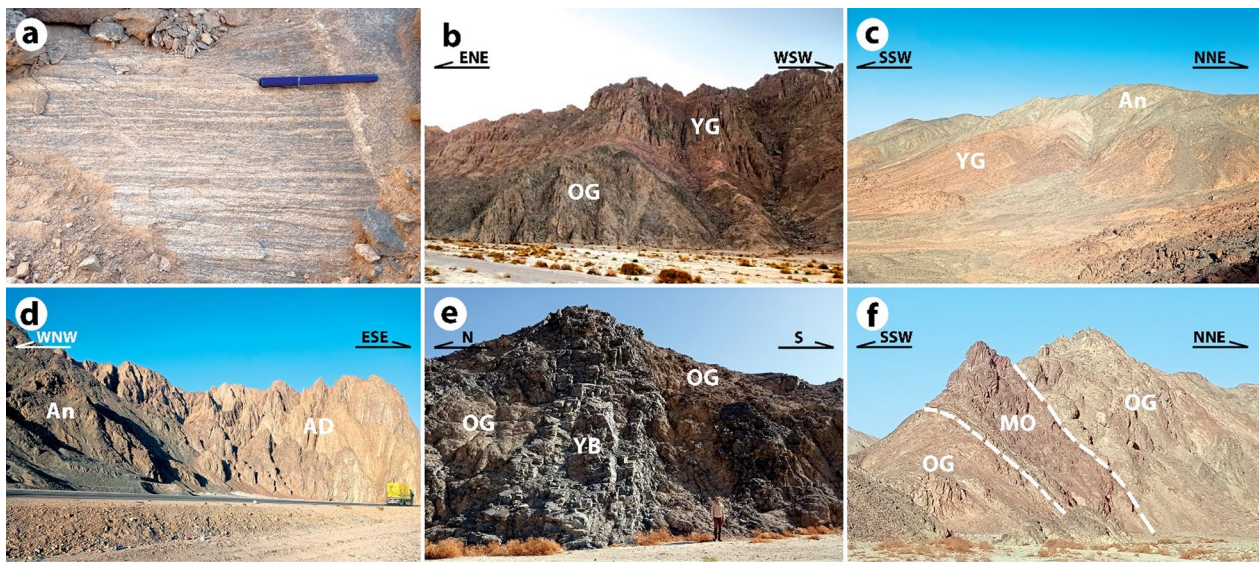
Fig. 12 Field photographs, **a** close-up view showing gneissic and migmatitic structures in older granitoids. **b** Intrusive contact between older granitoids (OG) and younger granites (YG) of G. Um Taghir El Tahtani. **c** Large roof-pendant of andesites (An) above younger granites (YG) at W. Nuqara. **d** Intrusive contact between andesites (An) and acidic Dokhan volcanics (AD) at G. Nuqara. **e** Offshoots of younger gabbros (YB) invade older granitoids (OG) at W. Abu Hadeida. **f** Microgranitic offshoot (MO) intrudes older granitoids (OG) at W. Ras Abda

3.2.2.2 Joint analysis The analysis treatment of the measured joints (Fig. 15) revealed that E–W, NNE–SSW and NE–SW are the main joint sets constituting 19.4%, 16.4% and 16% of the total number proportions of joints, respectively. They are followed by ENE–WSW and NNW–SSE sets, while WNW–ESE, N–S and NW–SE trends represent the minor ones.

3.2.2.3 Dyke and vein analysis   From the statistical analyses of the measured dykes and veins (Fig. 16), it can be noticed that most of dykes and veins follow E–W, WNW–ESE and ENE–WSW as master trends, followed by NE–SW and NW–SE directions. This is besides NNW–SSE, NNE–SSW and N–S as minor trends.

Based on remote sensing results, field observations and petrographic studies, a detailed geologic map is constructed (Fig. 17) in order to identify, classify and chronologically arrange the exposed rock types in the study area. Main structures are constructed on it.

4 Discussion

In the present work, a carful investigation of the measured spectral signature curves as well as the resampled one (which based on the wavelength range of both Landsat-8 and Sentinel-2A data characteristics) for the rock units in the study area, this led to determination of the most sensitive bands characterized the rock types presented in the study area. Accordingly, the chosen sensitive bands used for developed five mathematical formulas applied on the remotely sensed imagery for lithological

discrimination. Generally, all resulted images show a very high accuracy. The developed band ratios were successfully differentiated among all the exposed rock types on the processed Landsat-8 and Sentinel-2A, while PCA did not show a clear differentiation between the older and younger granites on Sentinel-2A. Despite, it is still a good attempt for lithological mapping, where it was successful to discriminate all the exposed rock types on Landsat-8.

Field investigation was consistent with the remote sensing results for the occurrence of the different rock types and the relative contacts between them, constructing a detailed lithological map of the study area. Petrographic studies confirmed these results and were able to distinguish the three varieties of the older granitoids (quartz-diorites, tonalites and granodiorites) that field observation could not distinguish between them, because these rocks are intercalated with each other and grade into one another through gradational blurred contacts due to the slight variation in their mineralogical composition; therefore, it is usually difficult to detect exactly a mappable contact between the different varieties of the older granitoids and reliance was placed on the petrographic studies.

Although the intense structural deformation (W. Um Taghir) is considered the Egypt's largest fault shear zone separating two tectono-stratigraphic domains; NED and CED [15], applying different methods (manual and automated methods) to extract the geological lineaments on data with different spatial resolution (geo-referenced Google Earth Pro images, panchromatic
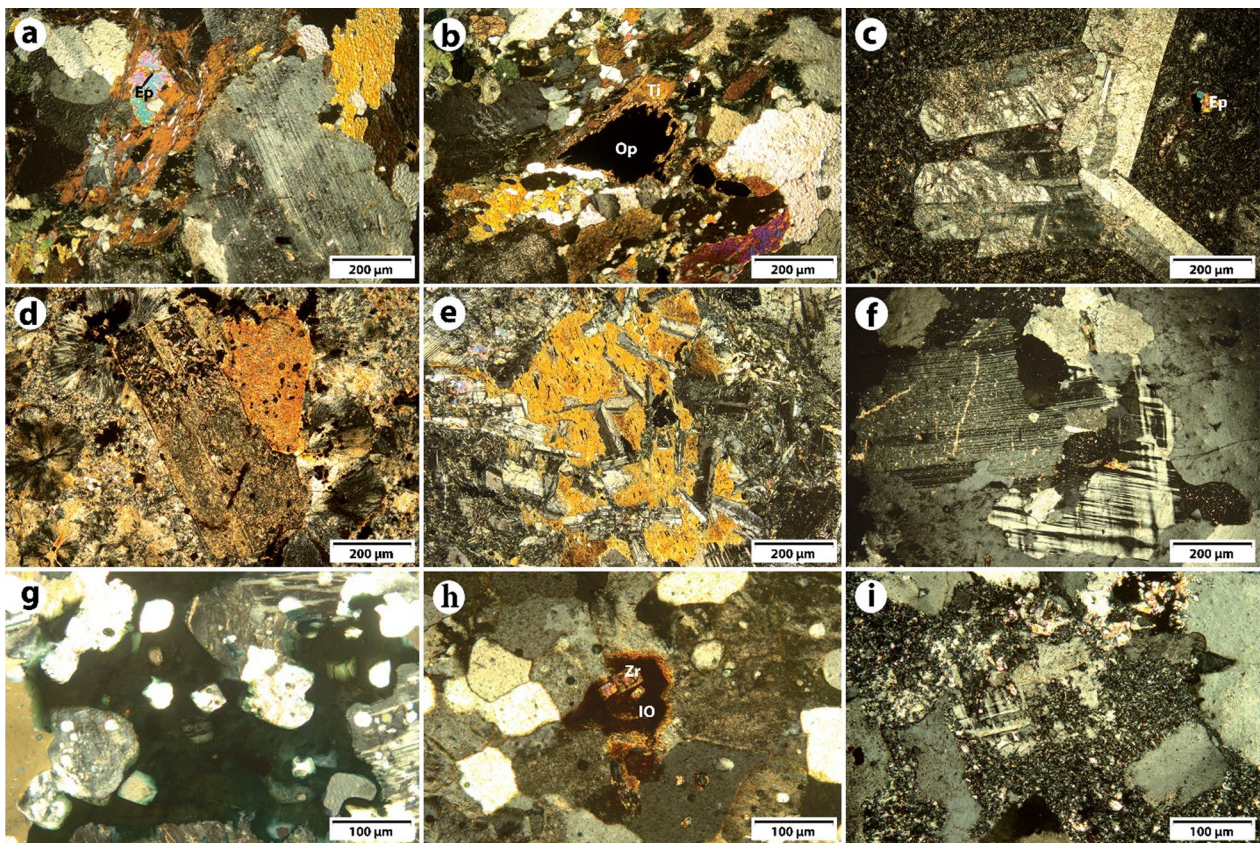
Salem *et al. Beni-Suef Univ J Basic Appl Sci*   (2024) 13:44

Page 18 of 22

Fig. 13 Photomicrographs, **a** Plagioclase crystal showing composed lamellar twinning and zonation associated with hornblende and epidote (Ep) in tonalites, C.N. **b** Opaques (Op) surrounded by secondary titanite (Ti) in tonalites, C.N. **c** Phenocrysts of plagioclase embedded in groundmass of quartz and epidote (Ep) displaying glomeroporphyritic texture in porphyritic andesites, C.N. **d** Plagioclase and associated minerals exhibiting porphyritic and spherulitic textures in rhyolites, C.N. **e** Prismatic crystals of plagioclase enclosed within hornblende displaying pseudo-ophitic texture in younger gabbros, C.N. **f** Plagioclase and microcline perthite displaying lamellar and cross-hatched twinning, respectively, in syenogranites, C.N. **g** Anhedral crystal of riebeckite showing blue interference color in alkali-feldspar granites, C.N. **h** Iron oxides (IO) included euhedral crystals of zircon (Zr) and surrounded by perthite and quartz in alkali-feldspar granites, C.N. **i** Silicification of syenogranites with relics of microcline in microgranites, C.N

band of Landsat-8 and ALOS PALSAR DEM), results were consistent and precise determined the prevailing trend controlling study region. The statistical analyses of the structural field elements (faults, joints, dykes and veins) with the surface structural lineaments extracted from both—satellite imagery and ALOS PALSAR Digital Elevation Model—detected that the main structural trend controlling the study area is the E-W, followed by WNW-ESE and NE-SW directions, while NNW-SSE and N-S trends represent the least common. E-W trend is the master trend controlling the study area, which represents the prevailing tectonic trend in the NED of Egypt [25].

The results of remote sensing achieved compliance with the geologic investigation, detailed petrographic studies and structural investigation through distinctly differentiating the different rocks and extracting the structural lineaments for the geologic mapping. This indicates the accuracy of the remote sensing results and emphasizes

their importance and effective role in the lithological identification and structural mapping and also emphasizes the importance of use multi-approach investigation (in the present study; satellite imagery data, field data and petrographic data) to obtain qualified results.

The results of the present study were consistent with previous studies in terms of the prevailing structural lineaments and the exposed rock units in the study area [5, 17, 25, 31]. However, integration of remote sensing technique, field and microscopic data proposed and applied in the current study was able to re-delineate the contacts among the different rock units, especially the contact between microgranites and older granitoids (Figs. 4, 6, 7) renovating a new and more precise extension of high rugged microgranites. The study also clearly distinguished between Dokhan volcanics (e.g., andesites, rhyodacites and rhyolites) and of younger granites (e.g., monzogranites, syenogranites and alkali-feldspar granites) (Figs. 4, 6,
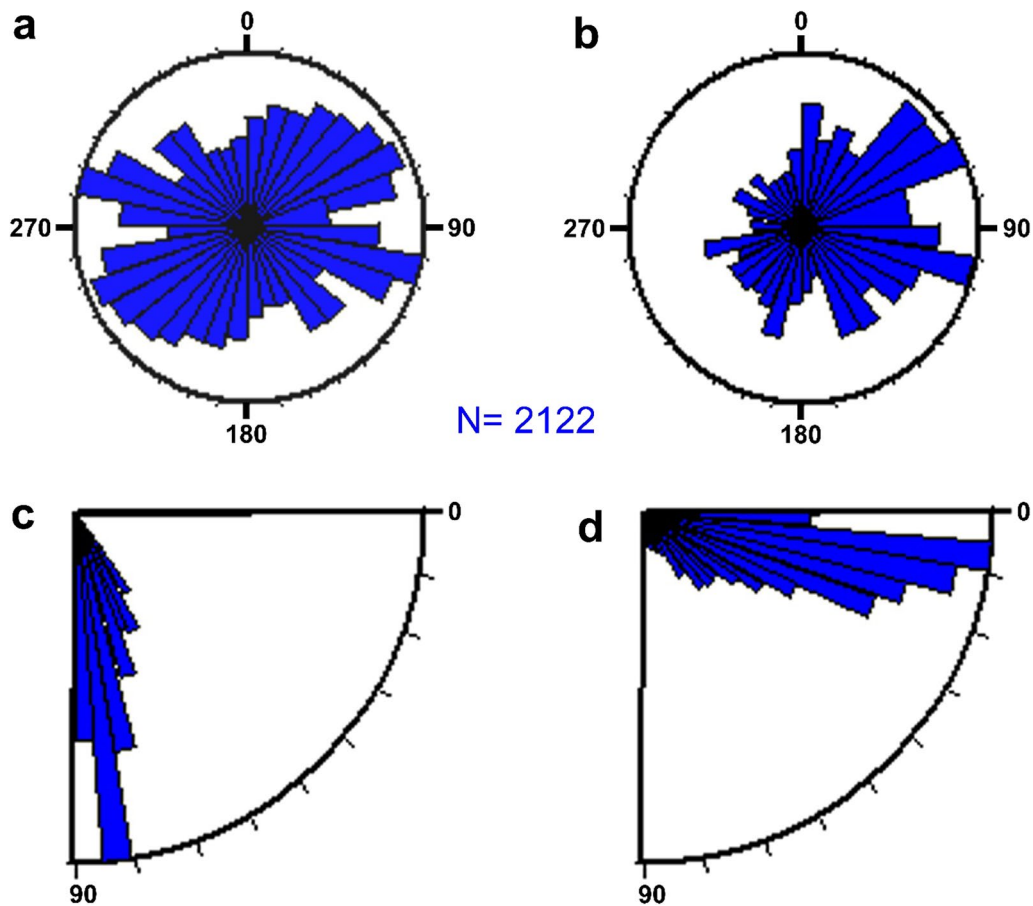
Fig. 14 Geometry of the measured faults in the study area, **a** strike trend. **b** Dip direction. **c** Dip angle. **d** Rake angle
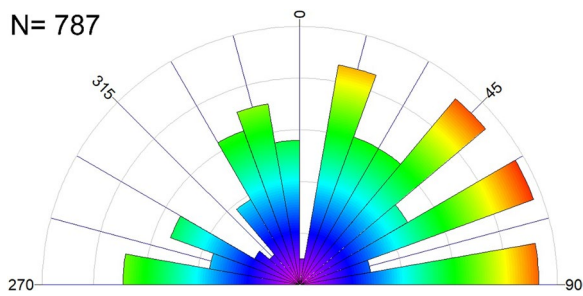

Fig. 15 Rose diagram of the measured joints in the study area based on their frequency distribution (*N*%)
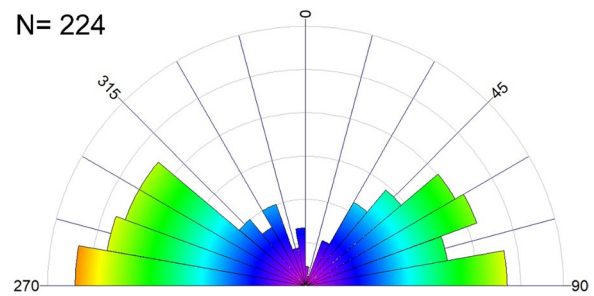

Fig. 16 Rose diagram of the measured dykes and veins in the study area based on their frequency distribution (*N*%)

7) and located the contacts between them with high quality, new geologic map (Fig. 17).

5 Conclusions

The following points can be concluded from the processing and interpretation of the remote sensing, geologic, petrographic and structural data used in this study:

1. Spectral signature curves and remote sensing data (Landsat-8 and Sentinel-2A) were used to create the most enhanced band combinations. The developed band ratios composites ((b7+b4)/(b7), (b2)/(b2+b5) and (b5) in RGB) for Landsat-8, and ((b9+b11+b12)/(b1), (b4-b2) and (b11/b6)+(b6) in RGB) for Sentinel-2A are the optimum composites
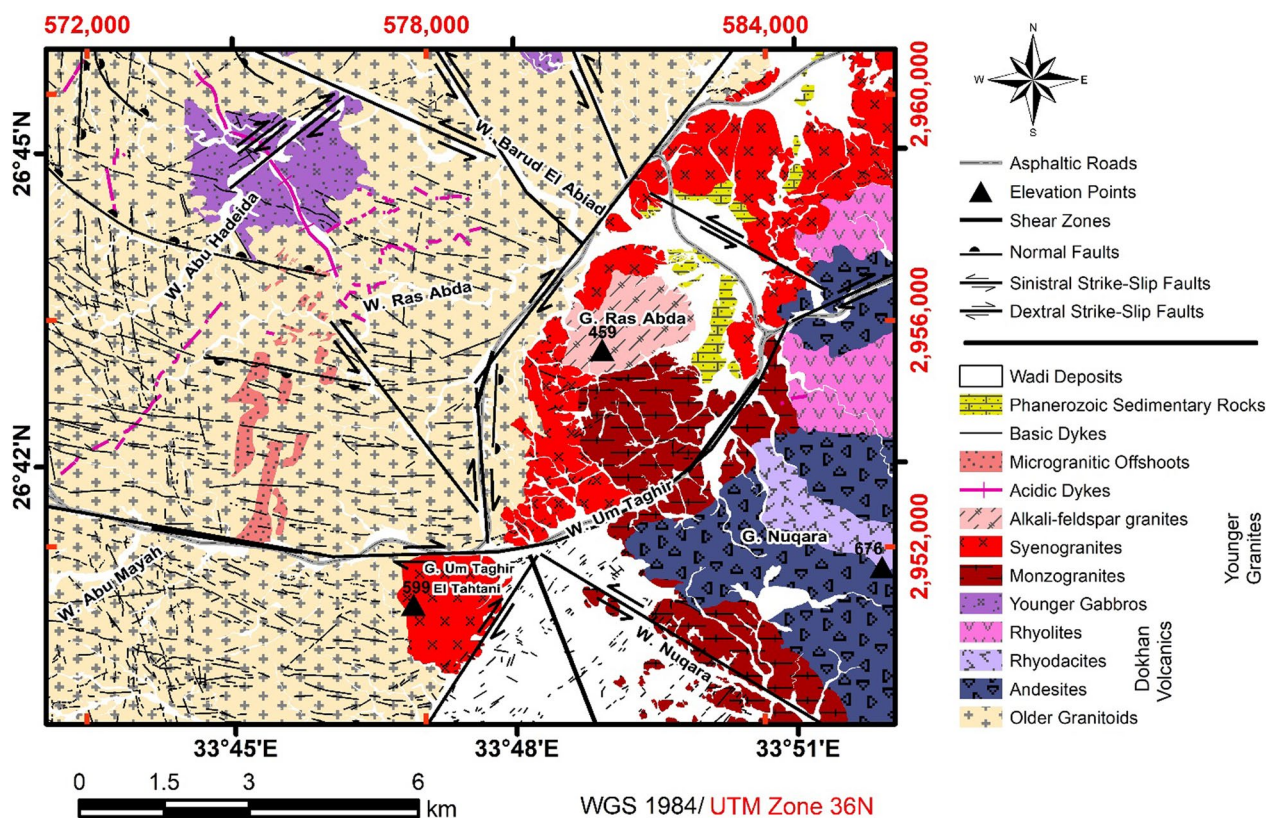
Fig. 17 Geologic map of G. Ras Abda area, northeastern desert, Egypt

to differentiate between all the exposed rock types in the study area.

2. Also, PCA presented a good attempt in discriminating the studied rocks, although it could not distinguish among the granitic varieties on Sentinel-2A image.

3. The main structural lineament trend controlling the considerable area is E–W followed by WNW–ESE direction, while the least common trends are represented by N–S and NNW–SSE. Moreover, the structural features are highly concentrated in the western parts of the study area.

4. The geologic and petrographic studies classified and arranged the studied rock types from the oldest to the youngest as follows: older granitoids (quartz-diorites, tonalites and granodiorites), Dokhan volcanics (andesites, rhyodacites, rhyolites and their related tuffs), younger gabbros, younger granites (monzo-granites, syenogranites and alkali-feldspar granites), post-granite dykes and offshoots (acidic, microgra
nitic and basic types) and Phanerozoic sedimentary rocks.

5. Also, the analysis of field structural elements (faults, joints, dykes and veins) revealed that E–W, WNW–

ESE, ENE–WSW and NE–SW are the main structural trends, while N–S, NNW–SSE and NW–SE trends represent the minor ones.

6. The results of remote sensing achieved compliance with the geologic, petrographic and structural investigation through distinctly differentiating the different rocks and extracting the lineaments, indicating the accuracy of the remote sensing results and emphasizing their importance and effective role in the lithological identification and structural mapping.

Abbreviations

b	Band no.
PC	Principal component
DEM	Digital elevation model
ANS	Arabian–Nubian Shield
EAO	East African Orogeny
NED	Northeastern Desert
CED	Central Eastern Desert
W.	Wadi (Vally)
G.	Gabal (Mountain)
ESA	European Space Agency
EMR	Electromagnetic radiation
FLAASH	Fast line-of-sight atmospheric analysis of spectral hypercubes
TOA	Top-of-atmosphere reflectance
SR	Surface reflectance
BR	Band ratios

Salem *et al. Beni-Suef Univ J Basic Appl Sci*　(2024) 13:44

Page 21 of 22

PCA　　　Principal component analysis
NIR　　　Near infrared
SWIR　　Short-wave infrared

Author contributions
MMS execute the field works/analysis, petrographic study, image processing and interpretation, writing the manuscript. MY contributed to image processing and interpretation, overall supervision, editing the `manuscript. AO contributed to field works/analysis, petrographic study, overall supervision, editing the manuscript. HS was involved in field works/analysis, petrographic study, overall supervision, editing the manuscript. MAS helped in assistance in the fieldworks. KA contributed to image processing and interpretation, overall supervision, editing the manuscript.

Availability of data and materials
The dataset used in the current study cannot be shared at present, because it is a part of ongoing Ph.D works. The dataset will be made available in the future upon request.

Declarations

Ethics approval and consent to participate
Not applicable.

Consent for publication
Not applicable.

Competing interests
The authors declare that they have no competing interests.

Author details
[1]Nuclear Materials Authority of Egypt, El Maadi, P.O. Box 530, Cairo, Egypt.
[2]Geology Department, Faculty of Science, Ain Shams University, Cairo, Egypt.

References

1. Abdel Ghani IM (2020) The application of Landsat-8 imagery and airborne gamma-ray spectrometric data for lithological mapping of Gabal Nuqara Area, Central Eastern Desert, Egypt. J North Basic Appl Sci 5(1):47–69. https://doi.org/10.12816/0055070
2. Abdelmalik KW (2020) Landsat 8: utilizing sensitive response bands concept for image processing and mapping of basalts. Egypt J Remote Sens Space Sci 23(3):263–274. https://doi.org/10.1016/j.ejrs.2019.04.004
3. Abdelmalik KW, Abd-Allah AMA (2018) Integration of remote sensing technique and field data in geologic mapping of an ophiolitic suture zone in western Arabian Shield. J Afr Earth Sc 146:180–190. https://doi.org/10.1016/j.jafrearsci.2017.10.006
4. Abu-Alam T, Santosh M, Brown M, Stüwe K (2013) Gondwana collision. Miner Petrol 107(5):631–634. https://doi.org/10.1007/s00710-013-0283-5
5. Awad HA, Abu El-Leil I, Kamel M, Tolba A, Nastavkin AV, El-Wardany RM (2022) Geological features identified from field observations and remote sensing data on the Um Taghir area, Eastern Desert, Egypt. Geodyn Tectonophys 13(3):1–23. https://doi.org/10.5800/GT-2022-13-3-0646
6. Awad HA, Abu El-Leil I, Nastavkin AV, Tolba A, Kamel M, El-Wardany RM, Rabie A, Ene A, Tekin HO, Issa SA, Zakaly HM (2022) Statistical analysis on the radiological assessment and geochemical studies of granite rocks in the north of Um Taghir area, Eastern Desert, Egypt. Open Chem 20:254–266. https://doi.org/10.1515/chem-2022-0131
7. Bencharef MH, Eldosouky AM, Zamzam S, Boubaya D (2022) Polymetallic mineralization prospectivity modelling using multi-geospatial data in logistic regression: the Diapiric Zone, Northeastern Algeria. Geocarto Int 37(10):1–31. https://doi.org/10.1080/10106049.2022.2097481
8. Delvaux D, Sperner B (2003) New aspects of tectonic stress inversion with reference to the TENSOR program. Geol Soc Lond Spec Publ 212:75–100. https://doi.org/10.1144/GSL.SP.2003.212.01.06
9. Dessouky OK, Sun W, Ibrahim WS, Ali HH, Hassan MM, Li C, Omran AA, Dardier AM (2021) New insights into Cryogenian arc granitoids hosting Th-U mineralized Ediacaran syenogranite dikes, Ra's Abdah area in the northern Egyptian Nubian Shield: constraints from U-Pb ages and zircon geochemistry. Precambr Res 352:1–18. https://doi.org/10.1016/j.precamres.2020.105986
10. El-Desoky HM, Tende AW, Abdel-Rahman AM, Ene A, Awad HA, Fahmy W, El-Awny H, Zakaly HMH (2022) Hydrothermal alteration mapping using Landsat 8 and ASTER data and geochemical characteristics of Precambrian rocks in the Egyptian shield: a case study from Abu Ghalaga, Southeastern Desert, Egypt. Remote Sens 14:1–30. https://doi.org/10.3390/rs14143456
11. Eldosouky AM, Elkhateeb SO, Ali A, Kharbish S (2020) Enhancing linear features in aeromagnetic data using directional horizontal gradient at Wadi Haimur Area, South Eastern Desert, Egypt. Carpathian J Earth Environ Sci 15(2):323–326. https://doi.org/10.26471/Cjees/2020/015/132
12. Eldosouky AM, Othman A, Saada SA, Zamzam S (2024) A new vector for mapping gold mineralization potential and proposed pathways in highly weathered basement rocks using multispectral, radar, and magnetic data in random forest algorithm. Nat Resour Res 33(1):23–50. https://doi.org/10.1007/s11053-023-10292-3
13. Eldosouky AM, Pham LT, El-Qassas RAY, Hamimi Z, Oksum E (2021) Lithospheric structure of the Arabian–Nubian shield using satellite potential field data. In: Hamimi Z et al (eds) The geology of the Arabian–Nubian shield. Springer Geology, Cham, pp 139–151. https://doi.org/10.1007/978-3-030-72995-0_6
14. Eldosouky AM, Sehsah H, Elkhateeb SO, Pour AP (2020) Integrating aeromagnetic data and Landsat-8 imagery for detection of post-accretionary shear zones controlling hydrothermal alterations: the Allaqi-Heiani Suture zone, South Eastern Desert, Egypt. Adv Space Res 65(3):1008–1024. https://doi.org/10.1016/j.asr.2019.10.030
15. El Gaby S, List FK, Tehrany R (1988) Geology, evolution and metallogenesis of the Pan-African belt in Egypt. In: El Gaby S, Greiling RO (eds) The Pan-African belt of Northeast Africa and adjacent areas. Vieweg & Sohn, Braunschweig, pp 17–68
16. El-Hadidy ShM, Alshehri F, Sahour H, Abdelmalik KW (2022) Detecting hydrocarbon micro-seepage and related contamination, probable prospect areas, deduced from a comparative analysis of multispectral and hyperspectral satellite images. J King Saud Univ Sci 34(6):102192. https://doi.org/10.1016/j.jksus.2022.102192
17. El-Mansi MM, Dardier AM, Abdel Warith A (2003) Geology and uranium distribution in Gabal Nuqara Dokhan volcanics, Central Eastern Desert, Egypt. Egypt J Geol 47(2):619–632
18. El Shazly EM, Dixon TH, Engel AEJ, Abdel-Meguid AA, Stern RJ (1980) Late Precambrian crustal evolution of Afro-Arabia from oceanic arc to craton. Egypt J Geol 24(1–2):101–121
19. Farag KSI, Howari FM, Abdelmalik KW (2019) Imaging of hydrothermal altered zones in Wadi Al-Bana, in southern Yemen, using remote sensing techniques and very low frequency–electromagnetic data. Arab J Geosci 12(18):1–16. https://doi.org/10.1007/s12517-019-4702-8
20. Fowler A, Baghdady A, Abdelmalik K, Gad A (2020) Remote sensing-guided stratigraphic dissection of an Ediacaran terrestrial molasse basin (Kareim basin, Egypt), with implications for sedimentary evolution. Precambr Res 338:105589. https://doi.org/10.1016/j.precamres.2019.105589
21. Ghoneim SM, Yehia MA, Salem SM, Ali HF (2022) Integrating remote sensing data, GIS analysis and field studies for mapping alteration zones at Wadi Saqia area, central Eastern Desert, Egypt. Egypt J Remote Sens Space Sci 25(1):323–336. https://doi.org/10.1016/j.ejrs.2022.02.001
22. Gomez C, Delacourt C, Allemand P, Ledru P, Wackerle R (2005) Using ASTER remote sensing data set for geological mapping, in Namibia. Phys Chem Earth 30:97–108. https://doi.org/10.1016/j.pce.2004.08.042
23. Guha A, Vinod Kumar K (2016) New ASTER derived thermal indices to delineate mineralogy of different granitoids of an Archaean Craton and analysis of their potentials with reference to Ninomiya's indices

for delineating quartz and mafic minerals of granitoids—an analysis in Dharwar Craton, India. Ore Geol Rev 74:76–87. https://doi.org/10.1016/j.oregeorev.2015.10.033

24. Hamimi Z, Abd El-Wahed MA, Gahlan HA, Kamh SZ (2019) Tectonics of the Eastern Desert of Egypt: key to understanding the neoproterozoic evolution of the Arabian–Nubian shield (East African Orogen). In: Bendaoud A et al (eds) The geology of the Arab world—an overview. Springer, Cham, pp 1–81. https://doi.org/10.1007/978-3-319-96794-3_1

25. Hamimi Z, Eldosouky AM, Hagag W, Kamh SZ (2023) Large-scale geological structures of the Egyptian Nubian Shield. Sci Rep 13:1–15. https://doi.org/10.1038/s41598-023-29008-x

26. Jemy G, Shokry MMF, Farag KSI, Abdelmalik KW (2023) Quadruple stacked-based concept: a novel approach for change detection. Int J Appl Earth Obs Geoinf 121:103361. https://doi.org/10.1016/j.jag.2023.103361

27. Johnson PR, Woldehaimanot B (2003) Development of the Arabian-Nubian Shield: perspectives on accretion and deformation in the northern East African Orogen and the assembly of Gondwana. Geol Soc Lond Spec Publ 206(1):289–325. https://doi.org/10.1144/GSL.SP.2003.206.01.15

28. Johnson PR, Andresen A, Collins AS, Fowler AR, Fritz H, Ghebreab W, Kusky T, Stern RJ (2011) Late Cryogenian-Ediacaran history of the Arabian–Nubian Shield: a review of depositional, plutonic, structural, and tectonic events in the closing stages of the northern East African Orogen. J Afr Earth Sci 61(3):167–232. https://doi.org/10.1016/j.jafrearsci.2011.07.003

29. Loughlin WP (1991) Principal component analysis for alteration mapping. Photogramm Eng Remote Sens 57:1163–1169

30. Mahdi AM, Eldosouky AM, El Khateeb SO, Youssef AM, Saad AA (2022) Integration of remote sensing and geophysical data for the extraction of hydrothermal alteration zones and lineaments; Gabal Shilman basement area, Southeastern Desert Egypt. J Afr Earth Sci 194:104640. https://doi.org/10.1016/j.jafrearsci.2022.104640

31. Omran AA (2014) Geology, mineralogy and radioelements potentialiyy of microgranite dikes to the south of Wadi Abu Hadieda area, Northern Eastern Desert, Egypt. Al Azhar Bull Sci 25(1):47–62. https://doi.org/10.21608/absb.2014.22610

32. Pohl W (1984) Large scale metallogenic features of the Pan-African in East Africa, Nubia and Arabia. Bull Fac Earth Sci Abdel Aziz Univ Saudi Arabia 6:591–601

33. Pour AP, Parsa M, Eldosouky AM (2023) Geospatial analysis applied to mineral exploration: remote sensing, GIS, geochemical, and geophysical applications to mineral resources. Elsevier, Amsterdam. https://doi.org/10.1016/C2021-0-02624-9

34. Sadiya TB, Abdulrahman A, Sadiq AA, Vaatyough HM, Ibrahim AT, Muhammed SO, Ihenacho NM, Yusuf MJ, Aliyu I, Agu NV (2016) Lineaments extraction from remote sensing data for detection of hydrothermal alteration zones in Northern Nigeria. IOSR J Environ Sci Toxicol Food Technol (IOSR-JESTFT) 10(4):17–22. https://doi.org/10.9790/2402-1004031722

35. Stern RJ (1994) Arc assembly and continental collision in the Neoproterozoic East African Orogen: implications for the consolidation of Gondwanaland. Annu Rev Earth Planet Sci 22:319–351

36. Vincent RK (1997) Fundamentals of geological and environmental remote sensing, 1st edn. Prentice Hall, Upper Saddle River. https://doi.org/10.1017/S0016756898391505

Publisher's Note

Springer Nature remains neutral with regard to jurisdictional claims in published maps and institutional affiliations.